Applied Composite Materials (2026) 33:128
https://doi.org/10.1007/s10443-026-10509-7

RESEARCH

Characterization and Modeling of the Time- and Temperature-Dependent Behavior of a Closed-Cell Polymer Structural Foam under Compression

Sarah Schlegel[1] · Eike Anton Schneider[1] · Martin Rosenschon[2] · Sascha Riegler[2] · Florian Wittemann[1] · Luise Kärger[1]

Received: 12 May 2026 / Accepted: 2 July 2026 / Published online: 21 July 2026

Abstract
The thermo-viscoelastic behavior of a closed-cell polyethylene terephthalate (PET) structural foam is investigated in order to accurately capture foam core deformations during manufacturing of composite sandwich structures, e.g. in Liquid Composite Molding (LCM), and their influence on the structural performance of the final components. The foam exhibits a transversely isotropic material behavior due to its manufacturing in the strand foam extrusion process. Compression tests are carried out in Dynamic Mechanical Analysis (DMA), where the heterogenous foam structure poses some difficulties in finding a valid measuring range and adequate parameter sets compared to a homogenous material. Therefore, close care is taken to select the right load range and sample size. In this way, the time- and temperature-dependency of the homogenized macroscopic material behavior of the structural foam is received. From the measured data, master curves are constructed using the time-temperature superposition principle and a temperature- and time-dependent prony series is fitted to the data. A non-isothermal modeling approach is proposed to capture the stiffness changes due to heating during the manufacturing process. The model is integrated into an open-source finite element framework and the underlying behavior is verified against a commercially available finite element model. The results show that the proposed model is able to accurately capture the thermoviscoelastic behavior of the foam under non-isothermal conditions.

Keywords Material modeling · Dynamic Mechanical Analysis (DMA) · Non-isothermal thermo-viscoelasticity · PET foam · Anisotropy · Sandwich manufacturing

✉ Sarah Schlegel
sarah.schlegel@kit.edu

[1] Institute of Vehicle System Technology - Lightweight Engineering, Karlsruhe Institute of Technology (KIT), Rintheimer Querallee 2, 76131 Karlsruhe, Baden-Württemberg, Germany

[2] Netzsch-Gerätebau GmbH, Wittelsbacherstr. 42, 95100 Selb, Bayern, Germany

1 Introduction

Structural polymer foams are gaining increasing recognition for their potential in sandwich structures due to their ability to reduce both weight and CO_2 emissions while maintaining adequate flexural stiffness. However, their behavior is complex, and achieving a targeted design of the manufacturing process and the structural performance of composite sandwich components requires a comprehensive understanding and modeling of the time- and temperature-dependent structural behavior of these foams.

Sandwich components can be manufactured in a single step using liquid composite molding (LCM) processes, where the foam core is placed between the face sheets in the mold, which are then impregnated with a resin. This process has the advantage of good interface bonding and higher stiffness of the sandwich components compared to a separate joining of core material and face sheets [1, 2]. Fischer Kerche et al. [3] examined the influence of different reinforcing fibers on the mechanical behavior of sandwich components with a PET foam core and mainly attributed the differences in the mechanical properties to morphological differences, such as resin pooling, that occur during vacuum infusion. This observation underscores the importance of understanding foam deformations during the manufacturing process. The fluid pressure during injection can lead to foam shifts and deformations that influence the manufacturing and the mechanical properties of the final components [4]. While these core deformations strongly influence the filling behavior [5], they are limited by the balance of forces between fluid and foam core as foam deformations lead to a larger fluid domain and thus, higher permeability of the facial sheets, reducing the fluid pressure on the core material. Numerical sensitivity studies also demonstrated significant interactions between foam core deformations and injection pressure, as well as an associated influence on the filling behavior in the LCM process [6, 7].

Under hydrodynamic pressure, thermoplastic foams exhibit a complex non-linear thermoviscoelastic-plastic behavior [8]. Especially strain rate and temperature strongly influence the material response. Quasi-static investigations of a closed-cell strand-extruded polyethylene terephthalate (PET) foam by AIREXhave been performed by Fathi [9] and Seuffert [7]. Seuffert [7] conducted uniaxial and hydrostatic compression tests, reporting orientation dependency in the extrusion direction and a strong reduction of mechanical properties once the glass transition temperature is surpassed. Similarly, Rezaei et al. [10] conducted shear and compression tests of a PET foam and sandwich components at elevated temperatures, also determining significant reduction in stiffness and strength near T_g of the polymer. Similar behavior was observed by Garrido et al. [11] and Mazzuca et al. [12] for other polymeric foams. In addition to foam density, temperature is identified as a primary factor influencing the material's mechanical behavior.

Jebur et al. [13] also used quasi-static compression tests to characterize the behavior of a melt-extruded closed-cell low-density polyethylene foam with special focus on the orientation dependency. They modeled the foam stiffness with a transversely isotropic hyperfoam model, reporting good agreement of the simulation results for arbitrary load angles with the corresponding experiments. Salloum et al. [14] conducted triaxial compression and shear tests on a PVC and a recycled PET structural foam. They found a good reproducibility of the tests and verified the assumption of transverse isotropic material behavior for the extruded foams. They adjusted the apparent material parameters found experimentally by numerical studies to account for multiaxial stress states.

The cell morphology of the strand-extruded PET foam series T92 by AIREX has been investigated by Fathi [9], who demonstrated that the process-induced cell structure significantly influences the anisotropy and mechanical properties of strand foams. These foams consist of hexagonal strands of varying sizes and exhibit differences in the wall thickness of the strand border zones.

Henriques et al. [15] investigated the viscoelastic shearing behavior of a closed cell polyurethane and an open-cell melamine foam focusing on the damping behavior of the polymeric skeleton. They used a four parameter fractional derivative model to numerically capture the shearing behavior. Daniel and Cho [16] characterized an anisotropic foam under static loading and with varying strain rates. They observed different characteristic stress peaks for different loading velocities but comparable material stiffnesses based on the initial slope. For numerical modeling they used a power law approach to correlate the initial stiffness and the foam density. A homogenized thermoviscoelastic model of PUR foam was proposed by Briody et al. [17] and compared to a hyperelastic Ogden model. They reported good agreement of the viscoelastic model with experimental results and conclude that the viscoelastic model was more stable for shear than the hyperfoam model and more suitable to capture reaction forces in indentation tests as stress relaxation occurs during the tests.

The thermoviscoelastic properties of thermoplastic closed-cell structural foams have been investigated in Dynamic Mechanical Analysis (DMA) by few authors in bending and compression mode. Garrido et al. [11] observed a continuous decrease in the storage modulus within the measured temperature range during dual cantilever mode testing, a typically expected behavior also for homogeneous materials. In contrast, DMA tests in compression mode conducted by Santo et al. [18] and Dietrich et al. [19] on PET foam and by Denay et al. [20] on PUR foam showed an increase in storage modulus with increasing temperature below the glass transition temperature. Santo et al. [18] attributed this increase to the collapse of foam cells, while Denay et al. [20] suggested that it is a structural effect driven by morphological changes within the foam. Dietrich et al. [19] ruled out some possible explanations like expansion of blowing agent residues and concluded that larger sample sizes and the loaded medium strain should be investigated further. Overall, the studies suggest that, for a thermomechanical analysis of thermoplastic foams, the experimental parameters and specimen sizes must be carefully selected in order to obtain valid results.

Modelling approaches for thermoviscoelastic behavior of homogenous polymers are well established, and the time-temperature superposition principle [21] is commonly used to derive master curves to fit the material behavior at different temperatures. However, for temperature-dependent modeling in non-isothermal processes, some common assumptions to simplify the equations cannot be made as easily because the relaxation times get time-dependent.

In this work, close care is taken to derive an adequate measuring range for the transversely isotropic time- and temperature-dependent material behavior of an extruded PET strand foam. The focus of this work is on a closed-cell polyethylene terephthalate (PET) foam by AIREX (namely foam AIREX T92.100).

Preliminary tests showed a significant effect of the foam structure during thermomechanical analysis. Based on these findings, an experimental setup suitable to capture the phenomenological behavior of the foam structure in forced oscillation is derived for dynamic mechanical measurements in compression. These measurements are used as basis for modeling the thermomechanical properties of the foam. For PET based foams the linear

viscoelastic behavior can be assumed dominant up to about 5% nominal strain [7]. During processing in LCM, depending on the infiltration pressure larger local strains can arise leading to plastic deformations or damage of the foam. However, both effects would lead to remaining defects in the sandwich component and are to be avoided by choosing adequate pressure limits during processing. These limits can be found for example by coupled LCM process simulations. For predicting the material behavior during processing in LCM until the start of plastic yielding or damage in the foam core, the strain and temperature dependency is assumed to be dominant over plastic deformations and a linear viscoelastic model is derived.

The focus of this work is on finding a suitable method for characterizing and, in particular, modeling and integrating thermomechanical behavior into an open-source framework for coupling with an LCM simulation. Thus, from the resulting temperature-frequency sweeps master curves at different temperatures are constructed using the Boltzmann superposition principle [21] and viscoelastic material parameters are identified based on the shifting and a reference master curve. The temperature-dependent model in a non-isothermal case is derived by a temperature shift of the relaxation times and an integral transformation to simplify the equations. This non-isothermal viscoelastic transversely isotropic model is integrated into an open-source framework that can be coupled to fluid mechanics simulations to capture the foam behavior during manufacturing of sandwich parts in LCM and its influence on the structural performance of the final components. To round things off, the underlying behavior of the derived material model is verified against commercial approaches.

2 Experimental Investigations

The foam under investigation is the T92.100 foam by AIREX, which is a PET structural foam with medium density of $100\,\mathrm{kg/m^3}$ manufactured in a strand foam extrusion process. Extruded strand foams typically show higher stiffness and strength in the extrusion direction than transverse to it because they exhibit a hexagonal honeycomb structure with elongated cells and aligned monomer chains in extrusion direction [9, 22, 23]. Therefore, at least three directions (in extrusion direction, transverse to it, and in 45° relative to the extrusion direction) have to be investigated to completely describe the foam behavior with a transversely isotropic model.

Viscoelastic behavior includes not only the properties of an elastic solid but also the properties of a viscous fluid [24], which means that the response of the material to a constant load is time-dependent [25]. Thus, the stress depends on the strain and strain rate and the time-dependent stress-strain relationship can be described by linear differential equations with constant coefficients [26]. The basis for the theory of linear viscoelasticity forms the theory of elastic aftereffects developed by Boltzmann [21], now commonly known as the Boltzmann superposition principle [27]. It states that strains can be added linearly and that the stress in the material at a certain point in time is a function of the strain history [21].

The viscoelastic material response can be measured by a dynamic mechanical analysis (DMA), also known as forced oscillation measurement [28]. In a DMA a sample is loaded by a static and dynamic load in order to determine the course of mechanical properties as a function of temperature, time and frequency [29]. The determined response signal of the

measurement is evaluated with regard to the phase shift δ between stress and strain and the respective amplitudes σ_A and ε_A [29].

It provides information about the complex modulus of elasticity $E^* = E' + iE''$, which can be calculated via the quotient of the stress and strain amplitude as

$$\|E^*\| = \frac{\sigma_A}{\varepsilon_A}. \tag{1}$$

It can be subdivided into its real part E' (storage modulus) and its imaginary part E'' (loss modulus).

For the polymeric foam under consideration, the hypothesis is proposed that the cell structure primarily influences the elastic stiffness components, while the time-dependent stiffness parts are predominantly determined by the base polymer and are therefore independent of orientation. This would imply that experiments in a single orientation would suffice. However, to verify this hypothesis, both the longitudinal and transverse directions are examined.

2.1 Preliminary Measurements and Motivation for Experimental Setup

In compression DMA of thermoplastic foams, unphysical increases in storage modulus with increasing temperature below the glass transition temperature have been observed by several authors [18–20]. This behavior is contrary to the expected behavior and was attributed to structural effects of the foam. However, the exact underlying mechanisms are not yet fully understood. Therefore, preliminary tests were conducted to investigate this behavior and to derive an adequate measuring range for the dynamic mechanical analysis of the PET foam under investigation.

The preliminary dynamic mechanical measurements were conducted on a DMA 242 E Artemis machine by Netzsch in compression mode. Due to the low force range of 12 N static and 12 N dynamic, the diameter of the cylindrical samples was chosen to be 7.5 mm to allow strains up to 1 % at forces below the maximum force of the device. The measurements were conducted in a temperature range from 293.15 K to 423.15 K and a frequency range from 0.1 to 10 Hz.

In alignment with literature, first measurements revealed an increase in the storage modulus with increasing temperature below the glass transition temperature (see Fig. 1) [18, 20]. Therefore, different studies were performed to investigate possible reasons for this unexpected behavior. As possible causes, the following were identified: (i) remaining blowing agent residues in the foam cells leading to additional expansion with increasing temperature, (ii) morphological changes in the foam structure leading to a structural stiffening, and (iii) local effects at the loading areas leading to high local strains and thus, a non-representative response of the foam structure. To further investigate these effects, three different foam densities of the same foam series (T92.80, T92.100, and T92.130) were investigated by Dietrich et al. [19], cyclic repetitions of the DMA measurements from cold to warm and back to cold were performed, samples were preliminary tempered [19], and samples were filled with a filler material to stabilize the open surface cells and to distribute the load more evenly into the foam structure.

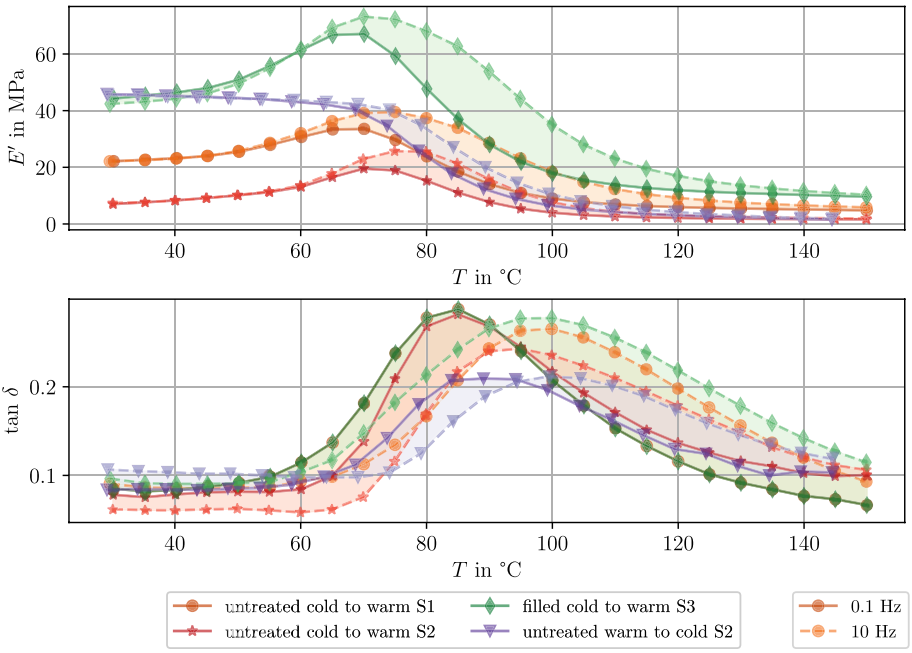

Fig. 1 Magnitude of storage modulus E' and loss factor $\tan\delta$ of the preliminary DMA measurements of T92.100 over Temperature T at frequencies 0.1 Hz (darker color) and 10 Hz (lighter color) investigated in step-wise isothermal mode every 5 K (data partly from [19]). All results for the intermediate frequencies lie within the shaded areas but are not explicitly represented to improve readability. Three different samples are depicted: Sample 1 (S1) is measured in step-wise isothermal mode from cold to warm temperatures [19], Sample 2 (S2) is measured in step-wise isothermal mode from cold to warm first and then reverse from warm to cold temperatures, Sample 3 (S3) is filled at the load introducing surfaces and measured from cold to warm temperatures in step-wise isothermal mode [19]. For Sample 2 it must be noted that the height was significantly reduced after the measurement due to foam collapse above T_g, explaining the monotonous rise of storage modulus with decreasing temperature in the backwards measurement. All samples are measured longitudinally to the extrusion direction

The different foam densities of the same foam series (T92.80 and T92.130) showed a similiar increase, however less pronounced [19], which could be attributed to different amounts of remaining blowing agent. Whether the effect is reversible or can be attributed to expansion of entrapped blowing agent residues or water or to cristallization effects, was investigated by cyclic repetitions of the DMA measurements going from low to high and back to low temperatures. The results of cyclic tests with unloading during cool-down showed that the increase in storage modulus persisted over several runs [19], whereas the increase vanished for measurements starting at high temperatures and cooling down (Fig. 1, Sample 2). In these cases the foam structure collapsed significantly during loading above T_g leading to a monotonous stiffness behavior over time. To separate those effects, preliminary tempered samples were investigated, showing that the increase in storage modulus with increasing temperature below T_g persisted even after tempering the samples at 150 °C for 116 h [19].

Tests were also conducted transverse to the extrusion direction to investigate whether the effect is direction-dependent and could therefore be attributed to reordering of polymeric

chains. However, the increase in storage modulus with increasing temperature below T_g persisted in transverse direction as well [19].

Thus, local effects at the load introduction remain as possible reason. The PET foam under investigation was previously studied in quasistatic and hydrostatic compaction tests by Seuffert [7], showing a starting range in quasistatic tests, where only a slight increase in stress with increasing strain can be observed. This starting range was not observed in hydrostatic compression tests of the same material [7]. Thus, it seems, that in uniaxial compression at first, only the surface of the sample is compacted. Only after reaching a strain of about 1 %, the load is distributed throughout the foam structure. High local deformations in the upper and lower boundary areas of a polymeric foam under compression were also observed by Rajput et al. [30]. However, in the preliminary tests the overall maximum strain (static and dynamic combined) was only 1 %, lying within the starting-range. To see whether the load distribution into the foam structure could be improved, samples were filled with a filler material (polyester resin based) to stabilize the open surface cells and to distribute the load more evenly into the foam structure. However, the increase in storage modulus with increasing temperature below T_g persisted (Fig. 1, Sample 3) [19].

In Fig. 1 it can also be observed that the initial stiffness differs significantly between two samples measured in the same way (Sample 1 and Sample 2). This indicates that the samples are too small to ensure representative results for the foam structure. It is concluded that the small sample size led to high local deformations at the loading areas, which influenced the measurement results significantly. Moreover, strains above 1 % should be chosen to avoid the start-up range identified by Seuffert [7]. Therefore, a new experimental setup is developed in the following section to rule out these effects and to ensure representative results for the foam structure under cyclic compression.

2.2 Experimental Setup

Based on the analysis of the preliminary tests, in the experimental setup it is ensured to measure in a strain range above the start-up range of the quasistatic tests. This strain range was secured by strain sweeps to ensure linear viscoelasticity in the chosen range.

In addition, sufficiently large sample sizes should be chosen to rule out size effects. Denay et al. [20] found a minimum loading surface of $12 \times 12\,\mathrm{mm}^2$ in their work, from which a representative answer in compression and creep tests of polymeric foam could be observed. Rajput et al. [30] also suggest to use larger sample sizes for which the effect of local deformations near the load introduction is less dominant. They found that the width-to-height ratio should be smaller than one. Fathi [9] reported different cell structures and mechanical properties within the honeycomb structure (strand center cells) and between the strands (strand border cells) of strand-extruded foams.

As in the preliminary tests, cylindrical samples are chosen, because less compaction force is needed for the same strains compared to a rectangular sample with the same width to height ratio. Considering the cell sizes identified by Fathi [9] and after testing different sample sizes, a diameter of $17\,\mathrm{mm}$ and a height of $20\,\mathrm{mm}$ were found to be sufficiently large to meet size effects while maintaining necessary compaction forces small enough to investigate strains above 1%. To ensure that the samples contain a representative share of both strand border and strand center cells, the samples are cut out of a larger foam block in such a way that they always contain at least two strand borders.

Fig. 2 Sample holder of the NETZSCH DMA 503 Eplexor® in compression mode. A cylindrical AIREX® T92.100 foam sample with a diameter of 17 mm and a height of 20 mm is placed on the sample holder

The dynamic mechanical measurements were carried out with a high force DMA 503 Eplexor® 500 N from NETZSCH (Selb, Germany). This instrument is capable of performing dynamic mechanical measurements under dynamic loads up to 500 N and static loads up to 1500 N. For this series of measurements, a force sensor with a maximum capacity of 500 N was employed. Temperature-frequency sweeps of the PET foam were conducted in compression mode over a temperature range of 293.15 K to 423.15 K, with isothermal steps of 5 K. The clamping in compression mode is shown in Fig. 2.

To ensure thermal equilibrium within the sample, a heat transfer simulation of the sample based on the heat conductivity given in the data sheet by the manufacturer and a mass averaged specific heat of PET and air was performed. It showed that a homogeneous temperature distribution within the sample is reached after 150 s. Therefore, a holding time of 300 s was applied prior to the frequency sweeps at each temperature. The viscoelastic properties were determined across a frequency range of 0.1 to 10 Hz using 4 frequency points per decade. All experiments were performed in a strain-controlled mode. Based on the findings from literature, the static strain was set to 1 % and the dynamic strain amplitude was set to 0.4 %. In total, four samples were tested: two longitudinal to the extrusion direction and two transverse to it.

The number of samples selected limits the validity of the experiments regarding the reproducibility and variability of the thermomechanical properties with respect to different cell structures within the samples. Conclusions regarding the chosen experimental setup and the directional dependence of the thermomechanical properties can be drawn even with the limited data set. Furthermore, the development and parameterization of a material model can be carried out independently of the variation in properties. The instantaneous moduli of the foam structure will be scaled to literature data retrieved from statistically validated quasistatic tests. The measurement results are sufficient to achieve the objectives of this work of developing a characterization and, in particular, a modeling method for the thermoplastic foam. Measurements on additional samples would be necessary for a well-founded assessment of the reproducibility and of the property variations caused by the foam structure.

2.3 Experimental Results

From the temperature-frequency sweeps the complex modulus and the loss factor are determined at the investigated temperatures and frequencies as represented in Fig. 3 for the four

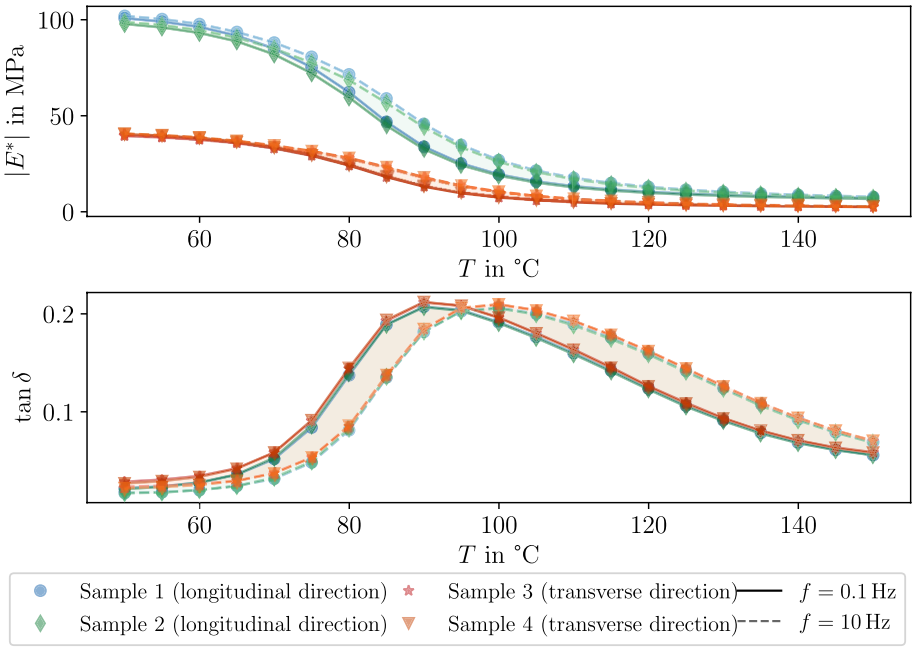

Fig. 3 Magnitude of complex modulus $|E^*|$ and loss factor $\tan\delta$ of the investigated samples of the PET foam T92.100 over Temperature T at frequencies 0.1 Hz (darker color) and 10 Hz (lighter color) investigated in step-wise isothermal mode every 5 K. All results for the intermediate frequencies lie within the shaded areas but are not explicitly represented to improve readability

investigated samples. To improve readability, only the course of the frequencies 0.1 Hz and 10 Hz is explicitly represented. All results for the intermediate frequencies lie within the shaded areas.

Contrary to the results reported in literature [18–20], the complex modulus monotonously decreases with increasing temperature. This behavior indicates that the choice of sample size and loading strain was suitable to achieve representative results for the foam structure under cyclic compression. The monotonous decrease aligns with the results in static testing of comparable polymeric foam structures, where a stiffness reduction at higher temperatures was reported [7]. Therefore, the measurements are considered to be suitable to capture the macroscopic temperature- and time-dependent behavior of the PET structural foam.

For the complex moduli a mean relative error (MRE) of 0.7 % is determined between the two samples measured in the longitudinal direction, and a MRE of 0.13 % is calculated between the two samples measured in the transverse direction. Thus, good agreement of the complex moduli of the samples measured in the same direction can be observed, indicating reproducibility of the experiments. Moreover, it can be observed that the magnitude of the complex modulus below the glass transition temperature is more than twice as high longitudinal to the extrusion direction than transverse to it. This behavior corresponds to the transversely isotropic behavior of strandextruded foams reported in literature [7, 9].

The loss factor shows a nearly identical behavior for all samples in both directions, indicating isotropy for the time-dependency of the material behavior. Quantitatively, for the loss factor a MRE of 0.15 % between the samples in the same direction and of 1.1 % between

the two directions is determined. This seems reasonable because the anisotropy of the material is caused by the foam structure while the time dependency is caused by the PET base material and is therefore likely to be independent of the cell structure. This will be further verified in the modeling process in section 3.1.

A shift of the glass transition range towards higher temperatures with increasing frequency can be observed in both the complex modulus and the loss factor. The glass transition temperature T_g is identified based on the loss factor to lie in between 87 °C and 99 °C, depending on the frequency. A summary of the basic material properties of the foam is given in Table 1.

2.4 Master Curve Construction

For the construction of master curves, it has to be verified first that linear thermoviscoelasticity can be assumed and the time-temperature-superposition principle [32] holds. Therefore, the loss modulus is plotted over the storage modulus in the Cole-Cole plot [33] in Fig. 4 for the measured frequency sweeps and temperatures. For temperatures above the glass

Table 1 Basic material properties of the investigated PET foam T92.100 by AIREX

Property	Value	Unit
Nominal density [31]	100	$\mathrm{kg/m^3}$
Glass transition temperature T_g	$87-99$	°C
Mean Young's modulus (compression), longitudinal [31]	90	MPa
Young's modulus (compression), longitudinal [9]	100	MPa
Young's modulus (compression), transverse [9]	30	MPa
Shear modulus longitudinal-transverse [31]	26	MPa
Shear modulus, transverse-transverse [9]	21.1	MPa
Thermal conductivity [31]	0.034	$\mathrm{W/m \cdot K}$

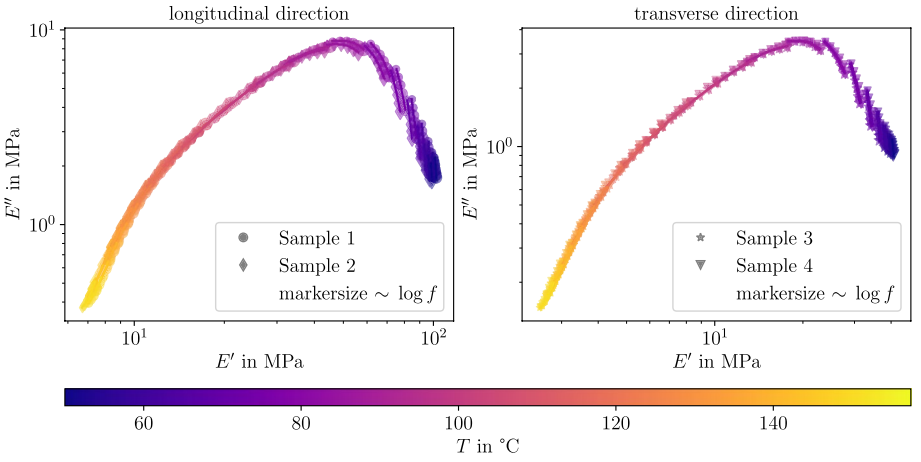

Fig. 4 Cole-Cole plot: loss modulus over storage modulus for the different tested temperatures and frequencies 0.1 Hz to 10 Hz obtained longitudinally (Samples 1 & 2) and transversely (Samples 3 & 4) to the direction of extrusion. Marker size scales with the logarithm of frequency, i. e. the smallest markers indicate $f = 0.1$ Hz and the largest markers indicate $f = 10$ Hz

transition temperature, a smooth progression of the relation can be observed. Below the glass transition temperature, slight offsets occur between the individual frequency sweeps. To a lesser extent, this also happens at temperatures above 50 °C, especially in the longitudinal direction. The effect is most pronounced at frequencies below 0.5 Hz.

Despite the carefully selected sample size, these offsets may still be attributable to edge effects caused by the cut, open-celled edge, which influences the results particularly under slow loading and at low temperatures, whereas at higher temperatures it softens sufficiently to have no further influence on the measured stiffness. In addition, the strain sweeps have shown that it is extremely difficult to find a range with a linear stress response in which oscillations can be performed, so even small deviations from this linear stress response could be the cause. For frequencies above 0.5 Hz, the shifts are small enough to be neglected for the construction of a master curve.

For temperatures below $50\ ^\circ\mathrm{C}$ the material behavior is not changing with temperature significantly since the individual frequency sweeps are basically on top of each other. Therefore, only temperatures above 50 °C and frequencies above 0.5 Hz are taken into account for the construction of a master curve. Vertical and horizontal shifting is necessary to obtain a smooth result. In the longitudinal direction, the data for Samples 1 and 2 do not match exactly at temperatures below the glass transition temperature. For this reason, in both directions master curves and shift factors are calculated individually for each sample and averaged afterwards.

The shift factors are calculated by arc length minimization [34] to construct a master curve at $90\,^\circ\mathrm{C}$, which is close to the glass transition temperature. They are then approximated using a Williams-Landel-Ferry (WLF) equation [35]

$$\log_{10} a(T) = -\frac{C_1\,(T - T_\mathrm{s})}{C_2 + T - T_\mathrm{s}}, \tag{2}$$

where T_s is the reference temperature from which the parameteres are shifted and C_1, and C_2 are fitting parameters.

However, this approximation is only valid above T_g [35]. To account for this restriction and to model the discontinuity at T_g [35], an Arrhenius type equation [34] is used to model the shift factors below T_g

$$\ln a(T) = \frac{E_\mathrm{a}}{2.303R}\left(\frac{1}{T} - \frac{1}{T_\mathrm{s}}\right), \tag{3}$$

where E_a is the activation energy and R is the universal gas constant.

The quality of the shift factor fit is exemplarily evaluated for Sample 1 in Fig. 5. The WLF fit matches the initial shift factors obtained by arc-length minimization reasonably well. However, the trajectory of the shift factors in the Arrhenius regime has a negative curvature contrary to the positive curvature of the Arrhenius fit. Consequently, the quality of the fit deteriorates quickly for lower temperatures, providing yet another reason for the temperature cutoff at 50 °C. For sufficiently high shift factors (at lower temperatures), the influence of the actual shift value on the stiffness decreases due to the exponential function. In the chosen temperature range, the fit is considered to meet the initial shift factors sufficiently well.

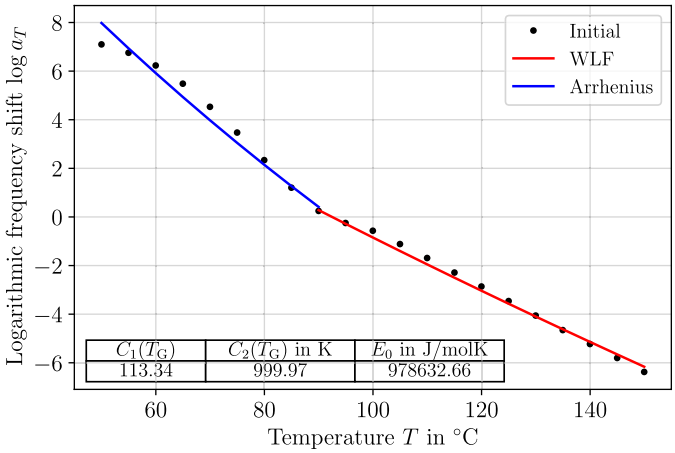

Fig. 5 Shift factors over temperature and corresponding fit with Arrhenius and Williams-Landel-Ferry (WLF) equation (Sample 1). Initial discrete shift factors for each temperature as obtained by arc length minimization are represented as black dots. The fitting parameters are given in the table on the bottom left

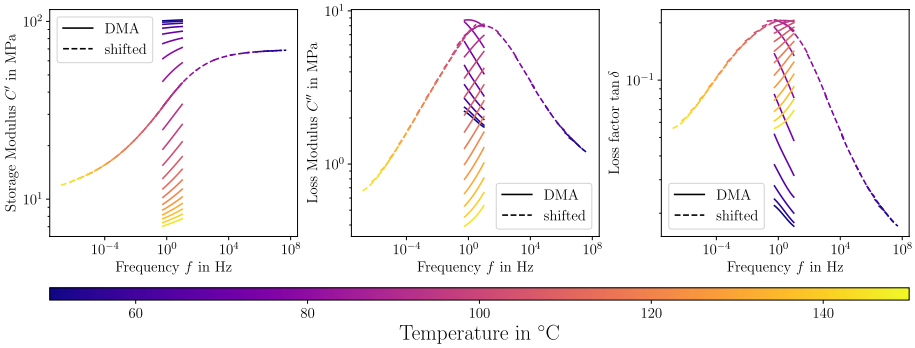

Fig. 6 Master curve construction: raw and shifted data (Sample 1) for storage modulus E', loss modulus E'' and loss factor $\tan\delta$ over frequency using the fitted WLF and Arrhenius equations

The resulting shift of the data is shown in Fig. 6. The master curve used in the further modeling is a polynomial interpolation of this shifted data.

3 Material Modeling and Verification

Based on the experimental results, a thermoviscoelastic material model is derived and parameterized. In the linear viscoelastic case, the components of the time-dependent stiffness tensor are commonly represented by a series and parallel connection of spring and dashpot elements, such as a parallel connection of N so-called Maxwell elements [36, 37]. This Generalized Maxwell Model (GMM) can be numerically represented by a Prony series, for which the stiffness can be formulated in a one-dimensional case as [38]

$$E(t) = \underbrace{E_0 \left(1 - \sum_{m=1}^{N} c_m\right)}_{E_\infty} + E_0 \left(\sum_{m=1}^{N} c_m \, \mathrm{e}^{-\frac{t}{\tau_m}}\right), \tag{4}$$

where $E_0 = E_\infty + \sum_{m=1}^{N} E_m$ is the instantaneous Young's modulus, $\tau_m = \frac{\eta_m}{E_m}$ are the relaxation times of the individual Maxwell elements and $c_m = \frac{E_m}{E_0}$ are the dimensionless so-called Prony coefficients. The Prony coefficients are the respective stiffnesses in a normalized form in each spring element, with $\sum_{m=1}^{N} c_m \leq 1$ to ensure the positivity of $E(t)$ at all times and thus, thermodynamic consistency. E_∞ is the long-term Young's modulus for $t \to \infty$, and E_m and η_m are the spring stiffnesses and dashpot viscosities of the individual Maxwell elements.

The time-dependent stress in the three-dimensional case is given by the time integration of the stiffness tensor C_{ijkl} and the strain rate

$$\sigma_{ij}(t) = \int_0^t C_{ijkl}(t-s) \frac{\partial \varepsilon_{kl}(s)}{\partial s} \mathrm{d}s \tag{5}$$

with the integration variable s, called hereditary integral [26].

The Boltzmann superposition principle is valid for polymers as long as the material structure remains unchanged over the duration of an experiment. This includes that no transformation processes such as crystallization in thermoplastics or microcracks may occur [39]. In polymeric materials, creep and relaxation processes occur as a result of the rearrangement of macromolecules or parts of molecules due to reorientation, sliding or displacement processes [40].

3.1 Identification of Model Parameters

The model parameters are identified in the frequency domain by fitting the Prony coefficients to the master curves. To start with, the data for the longitudinal and transverse direction are considered independently. Using the GMM, the storage modulus and loss modulus can be expressed as functions of circular frequency:

$$E'(\omega, T) = E_0(T) \left(1 - \sum_{m=1}^{N} c_m(T)\right) + E_0(T) \sum_{m=1}^{N} \left(c_m(T) \frac{\omega^2 (\tau_m(T))^2}{1 + \omega^2 (\tau_m(T))^2}\right) \tag{6}$$

$$E''(\omega, T) = E_0(T) \sum_{m=1}^{N} \left(c_m(T) \frac{\omega^2 (\tau_m(T))^2}{1 + \omega^2 (\tau_m(T))^2}\right) \tag{7}$$

The Prony coefficients are then determined at a constant temperature using SciPy's `minimize` method with the BFGS solver [41–44], a relative convergence criterion of 0.01 with a maximum of 1000 iterations, an initial guess for $E_0 = 1.1 \max(E'_{\mathrm{exp}})$ and $c_i = (\max(E'_{\mathrm{exp}}) - \min(E'_{\mathrm{exp}}) / \max(E'_{\mathrm{exp}}))$, and a least squares residual of the form [45, 46]

$$r = \alpha_{E'} \sum_{k=1}^{n_\omega} \left(\frac{E'_{\mathrm{GMM}}(\omega_k) - E'_{\mathrm{exp}}(\omega_k)}{E'_{\mathrm{exp}}(\omega_k)} \right)^2 + \alpha_{E''} \sum_{k=1}^{n_\omega} \left(\frac{E''_{\mathrm{GMM}}(\omega_k) - E''_{\mathrm{exp}}(\omega_k)}{E''_{\mathrm{exp}}(\omega_k)} \right)^2, \quad (8)$$

$$\alpha_{E''} = 1 - \alpha_{E'}, \quad (9)$$

where $\alpha_{E'}$ and $\alpha_{E''}$ are weighting coefficients, the index GMM indicates values obtained from the model at a specific temperature, and the index exp indicates values obtained from the corresponding master curve at that temperature derived from the DMA. The relaxation times are directly given by a fixed logarithmic distribution inferred from the master curve through

$$\tau_m \in \left[\frac{1}{\max \omega_k}, \quad \frac{1}{\min \omega_k} \right]. \quad (10)$$

The condition $\sum_{m=1}^{N} c_m \leq 1$ is ensured indirectly by imposing a penalty on the residual if the condition is not met during an optimization step.

GMMs at different temperatures can be calculated individually by first shifting the master curve to the required temperature, and then fitting the GMM to the master curve using the described procedure. The resulting instantaneous moduli and Prony coefficients in longitudinal and transverse direction are depicted in Appendix A in Figs. 12, 13, and 14, respectively. All of them vary by less than 0.2% in the regarded temperature range and thus, will be assumed to be independent of temperature for all further modeling, incorporating temperature dependency only in the relaxation times. With this assumption, it is possible to calculate the model behavior at an arbitrary temperature solely by shifting the relaxation times. For the shifting, the master curve shift factors obtained from the Arrhenius (3) and Williams-Landel-Ferry (2) equations are used. The Prony coefficients and the instantaneous modulus are obtained by calculating a single Prony fit at a reference temperature. This leads to satisfactorily accurate results while minimizing model complexity and the number of necessary fitting parameters (compare Figs. 7(a), (b), and 8(a), (b)). The quality of the fit is evaluated by the coefficient of determination R^2 [46], given by

$$R^2 = 1 - \frac{\sum_{i=1}^{n_\omega} \left(E_i^{(\cdot)} - E^{(\cdot)}(\omega_i, E_0, c_m, \tau_m) \right)^2}{\sum_{i=1}^{n_\omega} \left(E_i^{(\cdot)} - \frac{1}{n_\omega} \sum_{i=1}^{n_\omega} E^{(\cdot)} \right)^2}, \quad (11)$$

where $R^2 = 1$ indicates a perfect fit. For simplicity, only the temperature mean of R^2 is shown.

A common span of relaxation times is used for the longitudinal and transverse directions. Due to differing sizes of the master curves' frequency spans, this can lead to artifacts on the edges of the approximated master curves if the limits for the relaxation times are set too tight and to too high shifting factors at lower temperatures for too broad limits. Taking the mean of the frequency extrema of the respective directions compromises between both effects

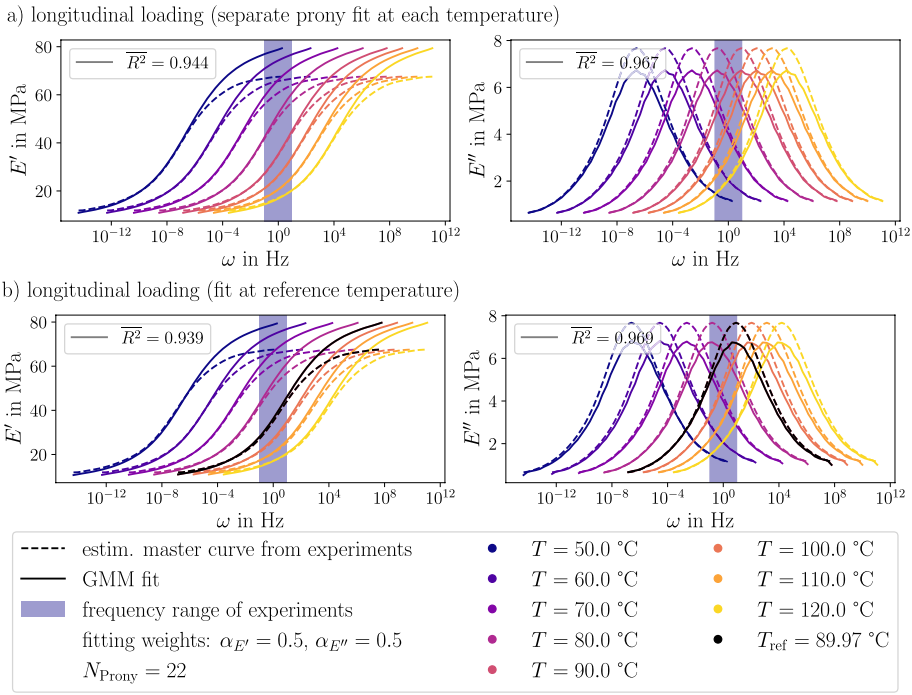

Fig. 7 Master curves and their approximation in the extrusion direction of the foam using a Prony series with separate fitting of Prony coefficients at each temperature (**a**) and using constant Prony coefficients fitted at a reference temperature with common relaxation time limits (**b**)

$$\tau_i \in \left[\frac{2}{\max \omega_k^{\text{longitudinal}} + \max \omega_k^{\text{transverse}}}, \quad \frac{2}{\min \omega_k^{\text{longitudinal}} + \min \omega_k^{\text{transverse}}} \right]. \quad (12)$$

Figure 9 shows the relative differences of the Prony coefficients in the longitudinal and transverse directions over the relaxation time spectrum at the reference temperature. Only for the four lowest relaxation times do their absolute magnitudes exceed 5%, and for the two lowest relaxation times 10%. This observation is consistent with the initial hypothesis that the time dependence of the material's behavior is direction-independent as observed in Fig. 3.

Consequently, a further simplification of the model is made by applying the Prony coefficients obtained for the longitudinal direction to both directions, discarding the Prony coefficients obtained for the transverse direction. Thus, the model parameters in the different directions only differ in the instantaneous modulus E_0.

In Fig. 8(b, c) it can be observed that this simplification produces a slight over-shift at lower temperatures for the storage modulus, as well as slightly worsens the fit for the loss modulus at high frequencies. Therefore, for low temperatures and load rates the storage modulus in transverse direction is slightly overestimated, making the material response a bit stiffer in transverse direction than it actually is. However, overall fit quality is only impacted by a decrease of R^2 by 0.01 for the storage modulus and 0.004 for the loss modulus, which is considered acceptable given the significant reduction in model complexity and

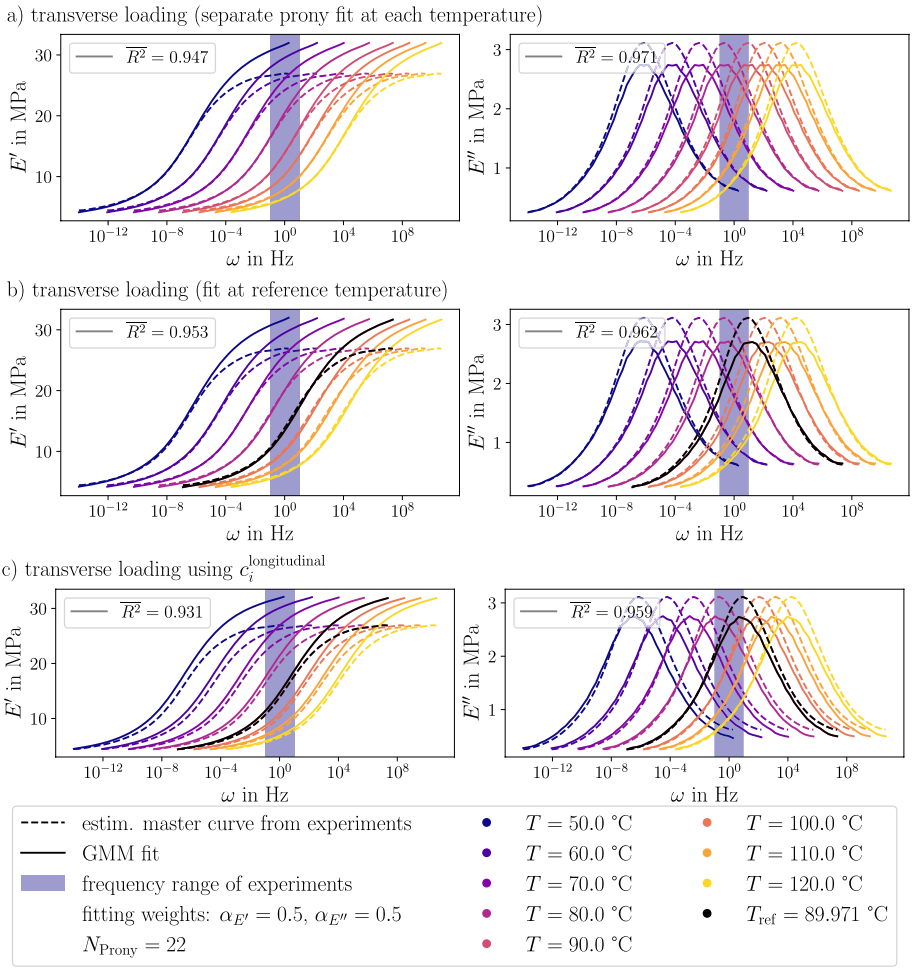

Fig. 8 Master curves and their approximation perpendicular to the extrusion direction of the foam using a Prony series with separate fitting of Prony coefficients at each temperature (**a**), using constant Prony coefficients fitted at a reference temperature with common relaxation time limits (**b**) and using the constant Prony coefficients obtained from the fit for the longitudinal direction (**c**)

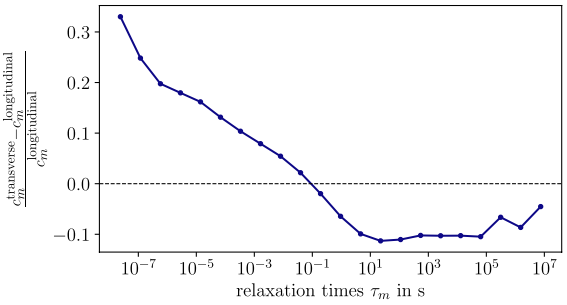

Fig. 9 Normalized differences between the Prony coefficients for the longitudinal and the transverse direction over their common relaxation times. Except for the Prony coefficients near the lower boundary of the spectrum, the deviation magnitude is less than 10%

the improved consistency of the model parameters across directions. The resulting fit of the loss factor $\tan\delta$ as calculated from the fits for E' and E'' is improved at low frequencies and worsened at large frequencies. Using a common set of Prony coefficients for both directions concurs with the observation that in the temperature-frequency-sweeps the profiles for $\tan\delta$ align almost perfectly and confirms the assumption of isotropic time-dependence (see Section 2.3).

In all variations of the model, the storage modulus at large frequencies is significantly overestimated by the GMM in both directions, while the heights of the peaks of the loss modulus and $\tan\delta$ are underestimated. In agreement with Kehrer et al. [46], it is observed that optimizing for a perfect fit of E' and optimizing for a perfect fit of E'' are conflicting objectives, with $\alpha_{E'} = \alpha_{E''} = 0.5$ yielding the best overall fit. It is also found that further increasing the number of Prony elements does not resolve this problem, instead only smoothing out the approximated curve.

3.2 Numerical Time Integration

Using the assumptions made in the previous section and the index notation for tensor representation $\underbrace{T_{ij}}_{\text{index notation}} = \underbrace{T_{ij}\mathrm{e}_i \otimes \mathrm{e}_j}_{\text{mixed notation}} = \underbrace{\mathrm{T}}_{\text{symbolic notation}}$, (4) can be generalized for the 3D case to

$$C_{ijkl}(t) = \underbrace{C^0_{ijkl}\left(1 - \sum_{m=1}^{N} c^m\right)}_{C^\infty_{ijkl}} + \sum_{m=1}^{N} \underbrace{C^0_{ijkl} c^m}_{C^m_{ijkl}} \mathrm{e}^{-\frac{t}{\tau_m}}. \tag{13}$$

The stress response of anisotropic viscoelastic materials represented by a Generalized Maxwell Model can be calculated from hereditary integrals [36, 47]

$$\begin{aligned}\sigma_{ij}(t) = &\underbrace{\int_0^t C^\infty_{ijkl} \frac{\partial}{\partial s}\left(\varepsilon_{kl}(s)\right) \mathrm{d}s}_{\sigma^\infty_{ij}(t)} \\ &+ \sum_{m=1}^{N} \underbrace{\int_0^t C^m_{ijkl} \exp\left(-\frac{t-s}{\tau_m}\right) \frac{\partial}{\partial s}\left(\varepsilon_{kl}(s)\right) \mathrm{d}s}_{\sigma^m_{ij}(t)},\end{aligned} \tag{14}$$

where $\sigma^m_{ij}(t)$ describes the stress in the m-th Maxwell element, and $\sigma^\infty_{ij}(t)$ the purely elastic stress response after an infinite loading time, which is represented by the spring element. $C^m_{ijkl}\mathrm{e}^{-t/\tau_m(T)}$ is the stiffness tensor in the m-th Maxwell element.

For non-isothermal processes the thermal expansion with thermal expansion coefficient tensor α_{ij} also has to be taken into account and the strain can be divided additively in a stress-dependent part ε^σ_{ij} and a temperature-dependent part $\varepsilon^{\mathrm{th}}_{ij}$. The part of the strain used for stress calculation is then given by

$$\varepsilon_{ij}^{\sigma} = \varepsilon_{ij} - \varepsilon_{ij}^{\mathrm{th}} = \frac{1}{2}\left(\frac{\partial u_i}{\partial x_j} + \frac{\partial u_j}{\partial x_i}\right) - \alpha_{ij}(T(s) - T_0). \tag{15}$$

Following the assumptions made during the parameter identification, the relaxation times τ_m depend on the temperature via

$$\tau_m(T) = a(T(t))\tau_m^{\mathrm{ref}}, \tag{16}$$

where the shift factor $a(T)$ is calculated according to (2) and (3) depending on the reference temperature used for the identification of the reference relaxation times τ_m^{ref}. Thus, the stress at an arbitrary time step t_p is given by

$$\begin{aligned}\sigma_{ij}(t_p) = &\underbrace{\int_0^{t_p} C_{ijkl}^{\infty} \frac{\partial}{\partial s}\left(\varepsilon_{kl}(s) - \alpha_{kl}(T(s) - T_0)\right) \mathrm{d}s}_{\sigma_{ij}^{\infty}(t_p)} \\ &+ \sum_{m=1}^{N} \underbrace{\int_0^{t_p} C_{ijkl}^{m} \exp\left(-\frac{t_p - s}{\tau_m(T(s))}\right) \frac{\partial}{\partial s}\left(\varepsilon_{kl}(s) - \alpha_{kl}(T(s) - T_0)\right) \mathrm{d}s}_{\sigma_{ij}^{m}(t_p)} .\end{aligned} \tag{17}$$

To calculate the stress in the m-th Maxwell element at the end of the increment $\Delta t = t_p - t_{p-1}$, the integral is divided into two time intervals $[0, t_{p-1})$, $[t_{p-1}, t_p]$, analogously to the derivation of Kiasat [48]. Since $\tau_m(T(s))$ depends on s in a general non-isothermal process, an integral representation of the exponential function

$$\exp\left(\frac{-(t_p - s)}{\tau_m(T(s))}\right) = \exp\left(-\int_s^{t_p} \frac{\mathrm{d}u}{\tau_m(T(u))}\right) \tag{18}$$

is introduced to transform the integral. A detailed derivation of the stress integration is given in Appendix B. For simplification of the stress components, three assumptions are necessary on the interval $[t_{p-1}, t_p]$, which hold in good approximation if the time increment is chosen sufficiently small:

1. The temperature T can be assumed to be constant during one time increment.
2. The components of the stiffness tensor C_{ijkl}^{m} are constant on the interval in good approximation.
3. The strain rate $\frac{\partial}{\partial s}\varepsilon_{kl}(s)$ is approximately linear on the interval and can therefore be simplified to $\frac{\Delta\varepsilon}{\Delta t}$ during one time increment.

As derived in Appendix B with these assumptions the stress increment at the end of the time step Δt can be expressed as

$$\begin{aligned}\Delta\sigma_{ij}(t_p) = \; & C_{ijkl}^{\infty}\left(\Delta\varepsilon_{kl}(t_p) - \alpha_{kl}(T(t_p) - T_0)\right) + \textstyle\sum_{m=1}^{N}\left[\exp\left(-\frac{\Delta t}{\tau_m(T(t_p))}\right) - 1\right]\sigma_{ij}^{m}(t_{p-1}) \\ & + \textstyle\sum_{m=1}^{N} C_{ijkl}^{m} \frac{(\Delta\varepsilon_{kl}(t_p) - \alpha_{kl}(T(t_p) - T_0))}{\Delta t}\tau_m(T(t_p))\left[1 - \exp\left(-\frac{\Delta t}{\tau_m(T(t_p))}\right)\right].\end{aligned} \tag{19}$$

Thus, the stress consists of a linear thermo-elastic part equivalent to Hooke's law and two thermo-viscoelastic parts. In the first viscoelastic part the stress history is taken into account by relaxing the viscoelastic stresses of the previous time step in each Maxwell element with the current relaxation times. The second viscoelastic part accounts for the change in viscoelastic stress in response to the current strain increment. Hence, the stresses at the end of the increment have to be cached for each Maxwell element as internal variables to be taken into account for the stress history in the next increment.

In a non-isothermal model, relaxation times can become high for low temperatures. Due to the splitting of the integral for the numerical approach, the viscoelastic stress contribution of the current strain increment in each Maxwell element is undefined for this behavior

$$\lim_{\tau\to\infty} C^m_{ijkl}\frac{\Delta\varepsilon_{kl}(t_p)}{\Delta t}\tau_m(T(t_p))\left[1-\exp\left(-\frac{\Delta t}{\tau_m(T(t_p))}\right)\right] = \infty\,[1-1]\,. \tag{20}$$

However, for large relaxation times the behavior should tend to a linear elastic material response

$$\lim_{\tau\to\infty} C_{ijkl}(t) = \lim_{\tau\to\infty} C^0_{ijkl}\left(1-\sum_{m=1}^{N} c^m\right) + C^0_{ijkl}\left(\sum_{m=1}^{N} c^m\,\mathrm{e}^{-\frac{t}{\tau_m}}\right) = C^0_{ijkl}, \tag{21}$$

and consequently, the viscoelastic stiffness contribution in each Maxwell element should tend to $C^0_{ijkl}c^m$. This is enforced in the implementation by checking the relaxation times in each Maxwell element and time increment. If it exeeds a certain threshold value, the stiffness is set to $C^0_{ijkl}c^m$ in the corresponding Maxwell element and time increment.

3.3 Verification of the Material Model

The derived and parameterized material model is implemented in the open-source Finite Element (FE) software `CalculiX` [49] as a user-defined material (UMAT). Open-source software has the advantage that coupling to different software is possible and more straightforward than with commercial tools. The derived material model shall be used in a coupled fluid-structure interaction (FSI) and conjugate heat transfer (CHT) simulation later on to capture the deformations of the foam material during processing of sandwich parts in liquid composite molding (LCM).

The relaxation behavior of the user-material is verified by comparison to a built-in model in the commercial FE-software Abaqus in a 3D coupled analysis: superimposing mechanical loading and temperature changes above T_g in all directions, considering transverse contraction and expansion. A cube is used as reference body, which is loaded at constant strain rate of 10 %/s in z-direction for 1 s in a first step (Fig. 10) in a coupled temperature-displacement analysis. The displacement is then held constant for 100 s to allow the stresses to relax. The transversal direction of the material is the x-direction.

Starting from an initial temperature of 370 K, a temperature of 400 K is specified on all surrounding surfaces to superimpose a thermal loading. For quantitative verification, a comparison to a built-in material model in the commerical software Abaqus is shown in Fig. 11.

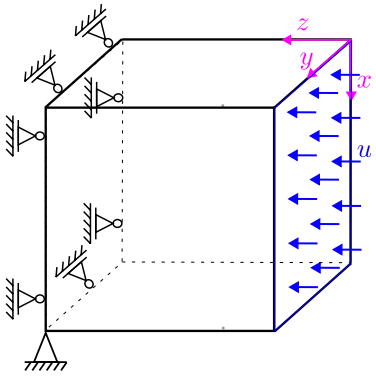

Fig. 10 Visualization of the mechanical loading and boundary conditions used for verification of the material model. The cube is clamped at one corner and translation in z-direction and rotations are locked at the maximum z-side (coordinate system depicted in pink) allowing for transverse motion in x- and y-direction. It is loaded by a constant displacement on the minimum z-side. The mechanical loadings are superimposed by temperature changes depending on the verification step

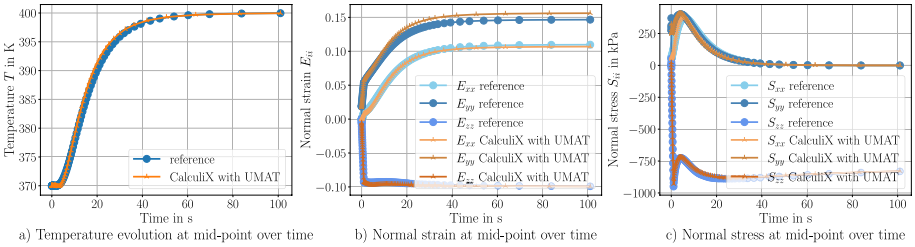

Fig. 11 Comparison of the non-isothermal 3D (**a**) temperature, (**b**) normal strain and (**c**) normal stress evolution over time at the node in the middle of the component. The reference simulation with the built-in Abaqus model is shown in blue against the `CalculiX` model with the user-defined material (orange). After one second of loading the displacement is kept constant for 100 s. At all surfaces the temperature is set to 400 K. Transversal contraction and temperature expansion are included in the simulations

To allow this comparison, the equilibrium and heating temperatures are chosen to be above T_g to allow modeling in Abaqus. Moreover, the size of the cube was chosen large enough, as to minimize surface effects on the stress evolution in the middle of the cube that occur for temperature dependent stiffnesses in Abaqus. The resulting temperature, strain evolution, and stress relaxation at a reference point in the middle of the cube are depicted in Fig. 11.

For the temperature evolution a mean absolute error (MAE) of 1.48 K is calculated, which corresponds to a mean relative error (MRE) of 0.38 %. The MAE for the strain is determied to be $5.12 \cdot 10^{-3}$ and 31.01 MPa for the stress. Thus,an overall good agreement of the temperature, strain and stress evolution can be noted with slight differences in strain caused by different time-stepping.

The x-direction is the extrusion direction of the foam, which is why different strain states arise in x- and y-direction of the sample. The z-direction is the load direction in which the highest nominal strains and stresses occur. A very high qualitative and quantitative agreement can be observed between the predictions of both programs. Only the normal strain in y-direction seems to be slightly overestimated by the derived open-source model, which can be attributed to the different time-stepping in both cases.

Overall, the verification demonstrates that the derived material model is able to capture the non-isothermal viscoelastic behavior of the foam material under the assumptions taken. For future work, a further validation with experimental data is planned in the context of LCM processing of sandwich parts to further validate the model for the intended application.

4 Conclusion

In this work, the linear thermoviscoelastic behaviour of a closed-cell PET structural foam was investigated and a macroscopic material model was developed and parametrized for usage in coupled manufacturing simulations of sandwich components. For this purpose, the time- and temperature dependent material response is assumed to be dominant. Large strains inducing plastic deformation or damage would cause persistent changes and thus, lead to resin-rich areas within the sandwich parts, which decrease the mechanical performance of the final components. Therefore, the model is limited to the linear viscoelastic regime to keep the model complexity as low as possible while still capturing the relevant material behavior for the intended application.

First, an adequate experimental setup was investigated in order to capture the time- and temperature dependent material response of the thermoplastic foam structure under compaction. Based on literature and preliminary tests, the usage of large enough samples and strains was identified to be crucial to prevent edge effects from influencing the measurement results and causing an unphysical increase in storage modulus with increasing temperature below T_{g}. The time-, temperature- and orientation-dependent material behavior was then macroscopically measured using dynamic mechanical analysis (DMA) with the identified testing parameters to ensure that the macroscopic behavior dominates. This led to a monotonously decreasing stiffness with increasing temperature for all tested frequencies suggesting that adequate testing parameters were chosen.

Measurements were conducted longitudinal and transverse to the extrusion direction of the foam material. While the storage modulus in longitudinal direction is about twice as high as in transverse direction due to the strand extruded cell structure, the loss modulus is similar in both directions. These results suggest that the time-dependence of the material is not direction dependent and that only the instantaneous properties have to be modeled anisotropically, which makes the three-dimensional material response much better predictable in practice, although a slight overestimation of stiffness in the transverse direction may occur. This assumption was verified by reconstructing master curves in transverse direction using the prony coefficients determined in longitudinal direction, which led to a sufficiently small deviation while reducing the amount of necessary parameters and the model complexity. Starting from one master curve in longitudinal direction and at one reference temperature, the temperature-dependence was incorporated into the relaxation times using an Arrhenius type equation below T_{g} and the WLF equation above T_{g}. In this way, the master curve can be shifted from the reference temperature to different temperatures which was verified by comparison to master curves constructed directly at exemplarily chosen temperatures.

Based on the discussed assumptions, a material model was derived using hereditary integrals and it was shown that common simplifications during integration hold true for non-isothermal processes. The resulting material model was incorporated in the open-source finite element framework `CalculiX`. This has the advantage of unrestricted accessibility independent of predefined user interfaces. Thus, it can for example easily be coupled to other simulation software, enabling the use of different numerical methods to solve structural mechanics and fluid mechanics in fluid-structure interaction problems. In the context of sandwich manufacturing, `CalculiX` can be coupled to the open-source toolbox `OpenFOAM` to capture the fluid-solid interaction of infiltrating resin and foam core deformations during manufacturing. The derived material model was verified by comparison to a built-in commercial model in `Abaqus` for homogenous materials. It could be demonstrated that the relaxation behavior and temperature dependence of the material stiffness can be correctly predicted using the derived model.

For the usage of the material model in manufacturing simulations of sandwich components no large strains are expected but rather high temperature changes for which the presented material model shows good predictions. For larger strains, damage and plastic deformation occur which are not captured by the presented linear thermoviscoelastic model to limit model complexity to the necessary minimum. Coupled process simulations capturing the fluid-structure interaction between mold-filling and foam core deformations based on the derived material model will be part of future research.

Appendix A: Prony Coefficients

In Fig. 12 the instantaneous moduli in extrusion direction and transverse to it are depicted over temperature for individual fits at each temperature. In Figs. 13, and 14 the corresponding relaxation times and the normalized change of the prony coefficients in extrusion direction and transverse to it are depcited, respectively. While the influence of temperature on the individual relaxation times is strong, the changes of the prony coefficients do not exceed 0.06%.

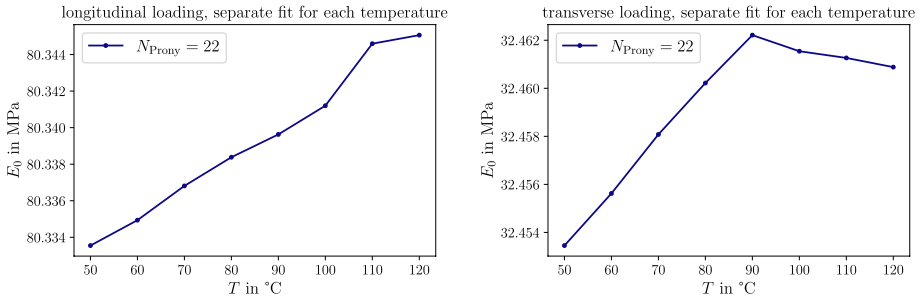

Fig. 12 Instantaneous modulus fitted at different temperatures for a GMM with 22 Prony elements in the direction of extrusion (longitudinal direction, left) and transverse to the direction of extrusion (transverse direction, right)

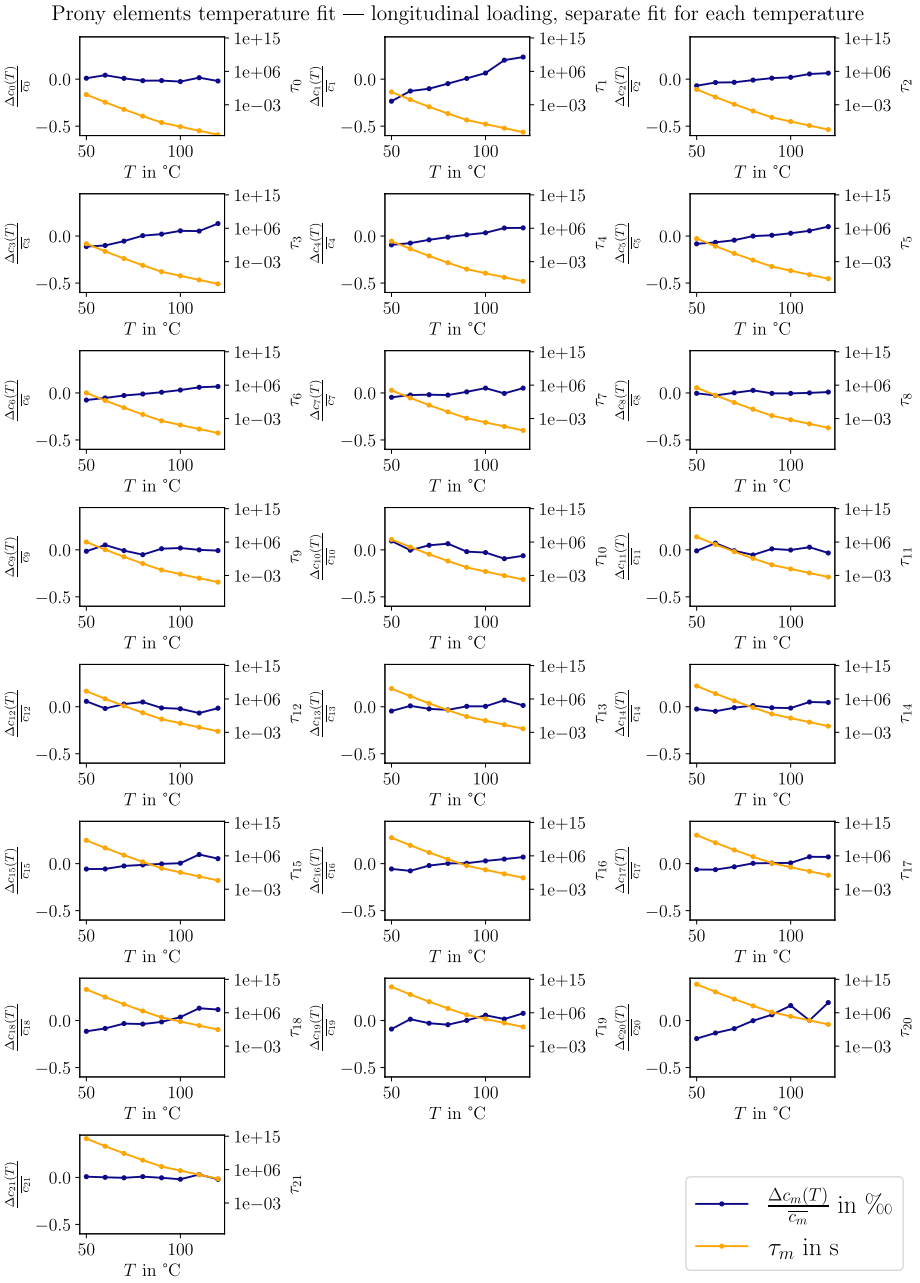

Fig. 13 Normalized change of Prony coefficients c_m and relaxation times τ_m fitted at different temperatures in each Maxwell element for a GMM with 22 Maxwell elements in the direction of extrusion

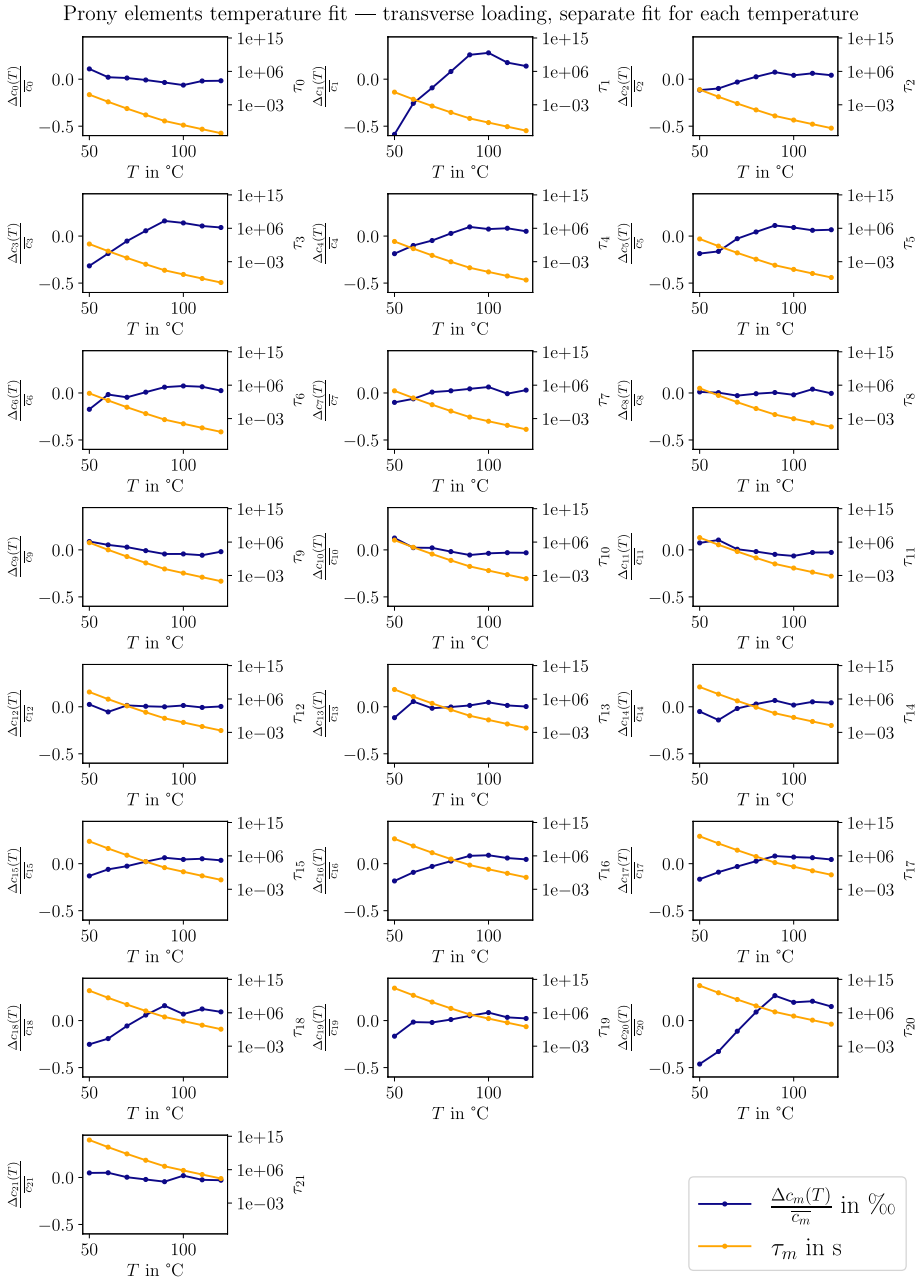

Fig. 14 Normalized change of Prony coefficients and relaxation times fitted at different temperatures in each Maxwell element for a GMM with 22 Maxwell elements transverse to the direction of extrusion

Appendix B: Model Derivation

Starting from the hereditary integral for the stress at an arbitray time t_p given in (17), the stress increment for a general non-isothermal process is derived in the following. Analogously to the derivation of Kiasat [48], the integrals are divided into two time intervals. For the elastic stress component in the single the partition yields

$$\begin{aligned}\sigma_{ij}^{\infty}(t_p) = &\underbrace{\int_0^{t_{p-1}} C_{ijkl}^{\infty} \frac{\partial}{\partial s} \left(\varepsilon_{kl}(s) - \alpha_{kl}(T(s) - T_0)\right) \mathrm{d}s}_{\sigma_{ij}^{\infty}(t_{p-1})} \\ &+ \int_{t_{p-1}}^{t_p} C_{ijkl}^{\infty} \frac{\partial}{\partial s} \left(\varepsilon_{kl}(s) - \alpha_{kl}(T(s) - T_0)\right)(s) \mathrm{d}s \\ =&\sigma_{ij}^{\infty}(t_{p-1}) + C_{ijkl}^{\infty} \left(\frac{\Delta\varepsilon_{kl}(t_p)}{\Delta t} - \frac{\alpha_{kl}(T(t_p) - T_0)}{\Delta t} \right) \int_{t_{p-1}}^{t_p} \mathrm{d}s \\ =&\sigma_{ij}^{\infty}(t_{p-1}) + C_{ijkl}^{\infty} \left(\Delta\varepsilon_{kl}(t_p) - \alpha_{kl}(T(t_p) - T_0)\right),\end{aligned} \tag{22}$$

which is equivalent to the constitutive equation in the linear thermo-elastic case. For the viscoelastic stress component in the *m*-th Maxwell the partition yields

$$\begin{aligned}\sigma_{ij}^{m}(t_p) \quad &= \textstyle\int_0^{t_{p-1}} C_{ijkl}^{m} \exp\left(-\frac{t_p - s}{\tau_m(T(s))}\right) \frac{\partial}{\partial s} \left(\varepsilon_{kl}(s) - \alpha_{kl}(T(s) - T_0)\right) \mathrm{d}s \\ &+ \textstyle\int_{t_{p-1}}^{t_p} C_{ijkl}^{m} \exp\left(-\frac{t_p - s}{\tau_m(T(s))}\right) \frac{\partial}{\partial s} \left(\varepsilon_{kl}(s) - \alpha_{kl}(T(s) - T_0)\right) \mathrm{d}s \\ &= \left(\sigma_{ij}^{m}(t_p)\right)^{I} + \left(\sigma_{ij}^{m}(t_p)\right)^{II}.\end{aligned} \tag{23}$$

It should be noted that $\left(\sigma_{ij}^{m}(t_p)\right)^{I}$ is not equivalent to $\sigma_{ij}^{m}(t_{p-1})$ due to the dependence on t_p instead of t_{p-1}. Since $\tau_m(T(s))$ depends on s in a general non-isothermal process, an integral representation of the exponential function is introduced in (18). Using the decomposition in two time intervals $t_p - s = (t_p - t_{p-1}) + (t_{p-1} - s)$, the integral can be split additively into

$$\int_s^{t_p} \frac{\mathrm{d}u}{\tau_m(T(u))} = \int_s^{t_{p-1}} \frac{\mathrm{d}u}{\tau_m(T(u))} + \int_{t_{p-1}}^{t_p} \frac{\mathrm{d}u}{\tau_m(T(u))} \tag{24}$$

and the exponential hence transforms to

$$\exp\left(-\int_s^{t_p} \frac{\mathrm{d}u}{\tau_m(T(u))}\right) = \exp\left(-\int_s^{t_{p-1}} \frac{\mathrm{d}u}{\tau_m(T(u))}\right) \cdot \exp\left(-\int_{t_{p-1}}^{t_p} \frac{\mathrm{d}u}{\tau_m(T(u))}\right), \tag{25}$$

where the second factor is independent of s. Consequently, the first part of the stress in the *m*-th Maxwell element simplifies to

$$\left(\sigma_{ij}^{m}(t_p)\right)^{I} = \underbrace{\exp\left(-\int_{t_{p-1}}^{t_p}\frac{\mathrm{d}u}{\tau_m(T(u))}\right)\int_0^{t_{p-1}} C_{ijkl}^{m}\exp\left(-\frac{t_{p-1}-s}{\tau_m(T(s))}\right)\frac{\partial}{\partial s}\left(\varepsilon_{kl}(s)-\alpha_{kl}(T(s)-T_0)\right)\mathrm{d}s}_{\sigma_{ij}^{m}(t_{p-1})}, \quad (26)$$

which analogously to the isothermal approach describes the stress history in each Maxwell element which is relaxed by the corresponding relaxation time at the current temperature.

For further simplification of the stress components, three assumptions are necessary on the interval $[t_{p-1}, t_p]$ as given in section 3.2. The first stress component $\left(\sigma_{ij}^{m}(t_p)\right)^{I}$ in each Maxwell element then simplifies to

$$\left(\sigma_{ij}^{m}(t_p)\right)^{I} = \exp\left(\frac{\Delta t}{\tau_m\left(T\left(t_p\right)\right)}\right)\sigma_{ij}^{m}(t_{p-1}), \quad (27)$$

which is the equivalent to the behavior in an isothermal approach. The stresses from the current strain increment are considered in the second integral $\left(\sigma_{ij}^{m}(t_p)\right)^{II}$ in each Maxwell element, for which the assumptions given in section 3.2 yield

$$\begin{aligned}\left(\sigma_{ij}^{m}(t_p)\right)^{II} &= C_{ijkl}^{m}\left(\frac{\Delta\varepsilon_{kl}(t_p)}{\Delta t}-\frac{\alpha_{kl}(T(t_p)-T_0)}{\Delta t}\right)\int_{t_{p-1}}^{t_p}\exp\left(-\frac{t_p-s}{\tau_m(T(s))}\right)\mathrm{d}s \\ &= C_{ijkl}^{m}\left(\frac{\Delta\varepsilon_{kl}(t_p)}{\Delta t}-\frac{\alpha_{kl}(T(t_p)-T_0)}{\Delta t}\right)\tau_m(T(t_p))\left[1-\exp\left(-\frac{\Delta t}{\tau_m(T(t_p))}\right)\right].\end{aligned} \quad (28)$$

The total stress at the end of the time increment results from addition of all components

$$\begin{aligned}\sigma_{ij}(t_p) = \; & \sigma_{ij}^{\infty}(t_{p-1}) + C_{ijkl}^{\infty}\left(\Delta\varepsilon_{kl}(t_p)-\alpha_{kl}(T(t_p)-T_0)\right) + \sum_{m=1}^{N}\left(\exp\left(-\frac{\Delta t}{\tau_m(T(t_p))}\right)\sigma_{ij}^{m}(t_{p-1})\right) \\ & + \sum_{m=1}^{N}\left(C_{ijkl}^{m}\frac{(\Delta\varepsilon_{kl}(t_p)-\alpha_{kl}(T(t_p)-T_0))}{\Delta t}\tau_m(T(t_p))\left[1-\exp\left(-\frac{\Delta t}{\tau_m(T(t_p))}\right)\right]\right).\end{aligned} \quad (29)$$

In consequence, the stress increment becomes

$$\begin{aligned}\Delta\sigma_{ij}(t_p) = \; & C_{ijkl}^{\infty}\left(\Delta\varepsilon_{kl}(t_p)-\alpha_{kl}(T(t_p)-T_0)\right) + \sum_{m=1}^{N}\left[\exp\left(-\frac{\Delta t}{\tau_m(T(t_p))}\right)-1\right]\sigma_{ij}^{m}(t_{p-1}) \\ & + \sum_{m=1}^{N} C_{ijkl}^{m}\frac{(\Delta\varepsilon_{kl}(t_p)-\alpha_{kl}(T(t_p)-T_0))}{\Delta t}\tau_m(T(t_p))\left[1-\exp\left(-\frac{\Delta t}{\tau_m(T(t_p))}\right)\right].\end{aligned} \quad (30)$$

Acknowledgements The funding by the German Research Foundation (DFG) within the project "Modeling of the fluid–structure interaction in mold filling processes for an intrinsic manufacturing of fiber-reinforced composite sandwich components (FSI-Sandwich)" (project no. 449100283) is gratefully acknowledged. The work is also part of the Heisenberg project "Digitalization of fiber-reinforced polymer processes for resource-efficient manufacturing of lightweight components," funded by the DFG, Germany (project no. 798455807141).

Author Contributions Sarah Schlegel: Conceptualization, methodology, software, validation, formal analysis, investigation, writing–original draft preparation, writing–review and editing, visualization, analysis and/or interpretation of data. Eike Anton Schneider: software, writing–original draft preparation, writing–review and editing, visualization. Martin Rosenschon: investigation, writing–review and editing,. Sascha Riegler: investigation, writing–review and editing. Florian Wittemann: writing–review and editing, supervision. Luise Kärger: Conceptualization, resources, writing–review and editing, supervision, project administration, funding acquisition. All authors have read and agreed to the final version of the manuscript.

Funding Open Access funding enabled and organized by Projekt DEAL.

Data Availability No datasets were generated or analysed during the current study.

Declarations

Competing interests The authors declare no competing interests.

References

1. Taghavian, S.H., Ghasemi, A.R.: The effect of manufacturing methods on the interface debonding and flexural behavior of sandwich structures: Thermography approach and three-point-bending Experiments. Polym. Compos. **43**(9), 6332–6343 (2022). https://doi.org/10.1002/pc.26942
2. Ahmadi, R., Wirawan, R., Judawisasastra, H.: Evaluation of facings and sandwich properties of carbon fiber/epoxy-PVC foam sandwich composites: Comparison of VARI co-cure and precure manufacturing methods. J. Sandwich Struct. Mater. 10996362241312871 (2025). https://doi.org/10.1177/10996362241312871
3. Fischer Kerche, E., Silveira Caldas, B.G., Carvalho, R.F., Amico, S.C.: Mechanical response of sisal/glass fabrics reinforced polyester – polyethylene terephthalate foam core sandwich panels. J. Sandwich Struct. Mater. **24**(6), 1993–2009 (2022). https://doi.org/10.1177/10996362221115057
4. Al-Hamdan, A., Rudd, C.D., Long, A.C.: Dynamic core movements during liquid moulding of sandwich structures. Compos. A Appl. Sci. Manuf. **29**(3), 273–282 (1998). https://doi.org/10.1016/S1359-835X(97)00082-1
5. Nedanov, P., Advani, S.G.: Mold filling simulation of sandwich composite structures manufactured by liquid molding: A parametric study. J. Sandwich Struct. Mater. **2**(2), 117–130 (2000). https://doi.org/10.1177/109963620000200202
6. Dietrich, S., Seuffert, J., Kärger, L.: Numerical investigation of the mold filling behavior of sandwich parts in resin transfer molding. In: Proceedings of the 23rd International Conference on Composite Materials (ICCM 2023) (2023). https://zenodo.org/records/15316800/files/ICCM23_Full_Paper_170.pdf
7. Seuffert, J.: Mold-filling simulation of resin transfer molding with fluid-structure interaction, Doctoral Thesis, Karlsruher Institut für Technologie (KIT). Karlsruhe (2022) https://doi.org/10.5445/IR/1000144393
8. Viot, P.: Hydrostatic compression on polypropylene foam. Int. J. Impact Eng **36**(7), 975–989 (2009). https://doi.org/10.1016/j.ijimpeng.2008.11.010
9. Fathi, A.: Mechanical properties of strand PET foams at different length scales, Universität Bayreuth (2018). https://doi.org/10.15495/EPub_UBT_00004286
10. Rezaei, M., Karatzas, V., Berggreen, C., Carlsson, L.A.: The effect of elevated temperature on the mechanical properties and failure modes of GFRP face sheets and PET foam cored sandwich beams. J. Sandwich Struct. Mater. **22**(4), 1235–1255 (2020). https://doi.org/10.1177/1099636218781995
11. Garrido, M., Correia, J.R., Keller, T.: Effects of elevated temperature on the shear response of PET and PUR foams used in composite sandwich panels. Constr. Build. Mater. **76**, 150–157 (2015). https://doi.org/10.1016/j.conbuildmat.2014.11.053
12. Mazzuca, P., Firmo, J.P., Correia, J.R., Castilho, E.: Mechanical behaviour in shear and compression at elevated temperature of Polyethylene Terephthalate (PET) foam. J. Build. Eng. **42**, 102526 (2021). https://doi.org/10.1016/j.jobe.2021.102526

13. Jebur, Q.H., Harrison, P., Guo, Z., Schubert, G., Ju, X., Navez, V.: Characterisation and modelling of a transversely isotropic melt-extruded low-density polyethylene closed cell foam under uniaxial compression. Proceed. Institut. Mechan. Eng., Part C **226**(9), 2168–2177 (2012). https://doi.org/10.1177/0954406211431528
14. Salloum, J., Léger, R., Chebbo, H., Daridon, L., Ienny, P.: A New methodology for the mechanical behavior analysis of polyvinyl chloride and recycled polyethylene terephthalate foams: finite element model updating using mechanical field measurements. J. Sandw. Struct. Mater. **26**(1), 73–93 (2024). https://doi.org/10.1177/10996362231203207
15. Henriques, I.R., Rouleau, L., Castello, D.A., Borges, L.A., Deü, J.-F.: Viscoelastic behavior of polymeric foams: Experiments and modeling. Mech. Mater. **148**, 103506 (2020). https://doi.org/10.1016/j.mechmat.2020.103506
16. Daniel, I.M., Cho, J.-M.: Characterization of anisotropic polymeric foam under static and dynamic loading. Exp. Mech. **51**(8), 1395–1403 (2011). https://doi.org/10.1007/s11340-011-9466-3
17. Briody, C., Duignan, B., Jerrams, S., Tiernan, J.: The implementation of a visco-hyperelastic numerical material model for simulating the behaviour of polymer foam materials. Comput. Mater. Sci. **64**, 47–51 (2012). https://doi.org/10.1016/j.commatsci.2012.04.012
18. Santo, L., Bellisario, D., Quadrini, F.: Shape Memory Behavior of PET Foams. Polymers **10**(2), 115 (2018). https://doi.org/10.3390/polym10020115
19. Dietrich, S., Dohmen, C., Frölich, F., Jackstadt, A., Wittemann, F., Kärger, L.: Investigation of the thermoviscoelastic behavior of a closed-cell polymer structural foam under pressure for processing in hybrid LCM processes. In: Binetruy C. (Eds) Proceedings of the 21st European Conference on Composite Materials, Vol. 2 Material Science, pp. 548 (2024). https://doi.org/10.5445/IR/1000173753/pub
20. Denay, A.-G., Castagnet, S., Roy, A., Alise, G.: Creep compression behaviour of a polyurethane foam from cryogenic temperatures: Size effect and long-term prediction. EPJ Web Conf **6**, 25006 (2010). https://doi.org/10.1051/epjconf/20100625006
21. Boltzmann, L.: Zur Theorie Der Elastischen Nachwirkung. In: Sitzungsberichte Kaiserliche Akademie Wissenschaft Wien Mathematisch-Naturwissenschaftliche Klasse, vol. 70, pp. 275–306 (1874)
22. Klempner, D., Aseeva, R.M., Sendijarevic, V.: Handbook of Polymeric Foams and Foam Technology, 2nd edn. Hanser, Munich (2004). ISBN 978-3-446-21831-4
23. Ramsteiner, F., Fell, N., Forster, S.: Testing the deformation behaviour of polymer foams. Polym. Test. **20**(6), 661–670 (2001). https://doi.org/10.1016/S0142-9418(00)00090-8
24. Lakes, R.S.: Viscoelastic Solids (1998), 1st ed., CRC Press Revivals, CRC Press, Boca Raton, FL (2017). https://doi.org/10.1201/9781315121369
25. Bertram, A. (collab. Glüge, R.).: Solid mechanics: Theory, modeling, and problems. Springer, Cham (2015. https://doi.org/10.1007/978-3-319-19566-7. ISBN 978-3-319-19565-0
26. Ferry, J.D.: Viscoelastic Properties of Polymers, 3rd edn. John Wiley & Sons, New York (1980). ISBN 0-471-04894-1
27. Schwarzl, F.: Polymermechanik: Struktur Und Mechanisches Verhalten von Polymeren. Springer, Berlin (1990)
28. Menard, K.P., Menard, N.R.: Dynamic Mechanical Analysis, 3rd ed., CRC Press, Boca Raton (2020). https://doi.org/10.1201/9780429190308. ISBN 978-0-429-19030-8
29. Ehrenstein, G.W., Riedel, G., Trawiel, P.: Praxis Der Thermischen Analyse von Kunststoffen. Hanser, München (2003). ISBN 3-446-22340-1
30. Rajput, M.S., Burman, M., Köll, J., Hallström, S.: Compression of structural foam materials - experimental and numerical assessment of test procedure and specimen size effects. J. Sandwich Struct. Mater. **21**(1), 260–288 (2019). https://doi.org/10.1177/1099636217690500
31. 3A Composites Core Materials: AIREX® T92 - Easy Processing Structural Foam: Data Sheet (2020). https://www.3accorematerials.com/uploads/documents/TDS-AIREX-T92-E-01.2020.pdf
32. Boltzmann, L.: Zur Theorie Der Elastischen Nachwirkung. Ann. Phys. **241**(11), 430–432 (1878). https://doi.org/10.1002/andp.18782411107
33. Cole, K.S., Cole, R.H.: Dispersion and absorption in dielectrics I. Alternating current characteristics. J. Chem. Phys. **9**(4), 341–351 (1941). https://doi.org/10.1063/1.1750906
34. Cho, K.S.: Viscoelasticity of polymers: Theory and numerical algorithms. Springer Science+Business Media, Dordrecht (2016). ISBN 978-94-017-7564-9
35. Williams, M.L., Landel, R.F., Ferry, J.D.: The temperature dependence of relaxation mechanisms in amorphous polymers and other glass-forming liquids. J. Am. Chem. Soc. **77**(14), 3701–3707 (1955). https://doi.org/10.1021/ja01619a008
36. Kaliske, M., Rothert, H.: Formulation and implementation of three-dimensional viscoelasticity at small and finite strains. Comput. Mech. **19**(3), 228–239 (1997). https://doi.org/10.1007/s004660050171
37. Pacheco, J.E.L., Bavastri, C.A., Pereira, J.T.: Viscoelastic relaxation modulus characterization using prony series. Latin Am J Solids Struct **12**(2), 420–445 (2015). https://doi.org/10.1590/1679-78251412

38. Barrientos, E., Fernández, F., Noriega, Á., Lamela, M.J., Fernández-Canteli, A., Tanaka, E.: Optimal discrete-time prony series fitting method for viscoelastic materials. Mechan. Time-Depend. Mater. **23**(2), 193–206 (2019). https://doi.org/10.1007/s11043-018-9394-z
39. Tobolsky, A.V.: Properties and Structure of Polymers. Wiley, New York (1960)
40. Huberth, H., Schirber, H., Schlör, N.: Kunststoffkunde: Aufbau. Eigenschaften, Verarbeitung, Anwendungen Der Thermoplaste, Duroplaste Und Elastomere, Vogel Business Media, Würzburg (2016). ISBN 3-8343-3366-2
41. Broyden, C.G.: The convergence of a class of double-rank minimization algorithms 1. Gen. Consider. IMA J. Appl. Math. **6**(1), 76–90 (1970). https://doi.org/10.1093/imamat/6.1.76
42. Goldfarb, D.: A family of variable-metric methods derived by variational means. Math. Comput. **24**(109), 23–26 (1970). https://doi.org/10.1090/S0025-5718-1970-0258249-6
43. Fletcher, R.: A new approach to variable metric algorithms. Comput. J. **13**(3), 317–322 (1970). https://doi.org/10.1093/comjnl/13.3.317
44. Shanno, D.F.: Conditioning of quasi-Newton methods for function minimization. Math. Comput. **24**(111), 647–656 (1970). https://doi.org/10.1090/S0025-5718-1970-0274029-X
45. Baumgaertel, M., Winter, H.H.: Determination of discrete relaxation and retardation time spectra from dynamic mechanical data. Rheol. Acta **28**, 511–519 (1989)
46. Kehrer, L., Keursten, J., Hirschberg, V., Böllke, T.: Dynamic mechanical analysis of PA 6 under hydrothermal influences and viscoelastic material modeling. J. Thermoplast. Compos. Mater. **36**(11), 4630–4664 (2023). https://doi.org/10.1177/08927057231155864
47. Flügge, W.: Viscoelasticity, 2nd rev. ed., Springer, Berlin (1975). ISBN 978-3-540-07344-4
48. Kiasat, M.S.: Curing shrinkage and residual stresses in viscoelastic thermosetting resins and composites, Ph.D. thesis, Technische Universiteit Delft, Delft (2000)
49. Dhondt, G.: The finite element method for three-dimensional thermomechanical applications. Wiley, Chichester (2004). ISBN 0-470-85752-8